Development of gum acacia based magnetic nanocomposite adsorbent for wastewater treatment

Prajwal Kulal
Mangalore University
Preetha B. Krishnappa
Mangalore University
Vishalakshi B (vishalakshi2009@yahoo.com)
Mangalore University

Research Article

Keywords: Gum acacia, Poly(3-chloro-2-hydroxypropylmethacrylate), Magnetite, Nanocomposite, Superparamagnetic property

Posted Date: April 21st, 2021

DOI: https://doi.org/10.21203/rs.3.rs-408981/v1

Development of gum acacia based magnetic nanocomposite adsorbent for wastewater treatment

Prajwal Kulal, Preetha B. Krishnappa, Vishalakshi Badalamoole*

Department of Post-Graduate Studies and Research in Chemistry,

Mangalore University, Mangalagangothri-574199 (D.K.), Karnataka, India.

e-mail: prajwal92kulal@gmail.com; preethakrishnappa@gmail.com;
*vishalakshi2009@yahoo.com

Abstract

Adsorbents fabricated on polysaccharides have captivated growing attention in water treatment owing to their low-cost and biodegradability. Modification of polysaccharides by incorporation of functional groups with potential binding ability towards pollutants is a good strategy to develop adsorbent materials. Imparting magnetic property to the materials facilitates easy separation of the adsorbent after use. The present work reports development of a magnetic hydrogel adsorbent material based on the polysaccharide, gum acacia. The graft copolymer nanocomposite hydrogel of gum acacia and poly(3-chloro-2-hydroxypropylmethacrylate) containing magnetite nanoparticles has been prepared using microwave assisted technique and evaluated as adsorbent for sequestration of cationic dyes and metal ions from aqueous solutions. The FTIR, XRD, SEM, TGA, VSM and BET studies have been performed to characterize the sample. The nanocomposite displayed super-paramagnetic nature owing to the existence of magnetite nanoparticles. The presence of magnetite nanoparticles is observed to influence the adsorption characteristics favourably as evident from the comparative studies performed with the non-magnetic parent gel. It exhibited larger surface area of 2.524 m^2g^{-1} compared to the parent hydrogel with surface area of 0.481 m^2g^{-1}. The adsorption capability of the parent hydrogel towards methylene blue, rhodamine 6G, Cu(II) and Hg(II) are 224.4, 283.5, 282.4 and 275.3 mgg^{-1} respectively are enhanced to 265.2, 344.4, 307.5 and 292.8 mgg^{-1} respectively in the case of nanocomposite. The adsorption isotherm and kinetic data fitted well with Freundlich and pseudo second order model respectively. Desorption studies indicated excellent reusability

characteristics of the novel adsorbent developed, indicating its potential use in wastewater treatment.

Key words: Gum acacia; Poly(3-chloro-2-hydroxypropylmethacrylate); Magnetite; Nanocomposite; Superparamagnetic property.

1. Introduction

The effluents of cosmetic, textile, leather, pharmaceutical, paper, plating and mining industries contain a wide variety of toxic dyes and metal ions. The existence of these contaminants beyond the acceptance limit result in adverse environmental impacts, which will have serious influence on human, plant and marine ecosystem [1,2]. The majority of synthetic dyes are mutagenic, toxic and carcinogenic in nature [3,4]. It is imperative to minimize the ecological impact of these effluents by declining the environmental footmark at every stage of their use. Therefore, several methods such as photo catalysis, ion-exchange, biological degradation, coagulation-flocculation, advanced oxidation processes, adsorption and membrane filtration have been adopted to reduce or minimize the pollution to a permitted level [5,6]. Among these methods, adsorption process was believed to be an effective method in comparison with other techniques due to its handy operation, low-cost, easy and rapid extraction and regeneration possibilities [7].

Nature affords an impressive range of polymers that have the potential to replace many synthetic polymers currently in use. Polysaccharides are naturally occurring organic macromolecules that are visualized as favorable alternatives of non-degradable synthetic polymers by virtue of their easy availability, low-cost, non-toxicity, biodegradability and biocompatibility [8,9,10]. Graft copolymerization is an outstanding technique to improve the properties of the polysaccharides. Grafting of vinylic and acrylic monomers on natural plant exudate polysaccharides has delivered some exciting strategies in fabricating hydrogels with high adsorption capacities [11,12,13,14,15]. Great progress has been made in recent years with concern to the preparation of polysaccharide based hydrogel nanocomposites. Production of nanocomposites from natural polymers is aimed at increasing the properties of the hydrogels and developing newer techniques with the view of sustainability of the environment. The utilization of hydrogels in the progress of nanostructured hybrid materials has abundant advantages in wastewater treatment [16,17,18,19,20,21].

Gum acacia or Gum arabic (GA) is a highly branched arabinogalactan polysaccharide exuded by acacia trees [22]. This carbohydrate molecule is composed by D-galactose, L-arabinose, L-rhamnose, D-glucouronic acid and 4-O-methyl-D-glucouronic acid units [23]. The structure and properties of GA could be easily tailored by introducing extra functional groups in the molecule through the –COOH and –OH groups present in its monosaccharide units. GA modified with vinyl monomers have been used earlier as adsorbents for the treatment of contaminated water. Sharma *et al.*, [24] fabricated a novel nanohydrogel of gum arabic and polyacrylamide using microwave assisted synthesis for adsorption of noxious crystal violet dye from aqueous medium. The highest adsorption capacity of crystal violet onto nanogel was found to be 90.9 mg g^{-1}. Abdel-Bary *et al.*, [25] studied graft copolymerization of polyacrylic acid onto gum acacia as a prospective candidate for removing of the dye methylene blue from aqueous system. Elbedwehy *et al.*, [26] reported development of a graft copolymer of polyacrylonitrile and gum acacia using $KMnO_4/HNO_3$ redox pair as initiator. The adsorbent exhibited super adsorbent ability with adsorption capacity of 1017, 413 and 396 mg g^{-1} for Pb^{2+}, Cd^{2+} and Cu^{2+} respectively.

The advent of nanotechnology has provided great opportunities for development of nanocomposite based adsorbents. Embedding magnetite nanoparticles (Fe_3O_4) in porous polymeric network of the hydrogel are attractive due to their recognized biocompatibility, sensitivity and rapid response to a remotely applied external magnetic field [27]. They can further expand the sorption capacity of hydrogel attributable to their nanoscopic size and the surface characteristics [28].

There are no reports available on the modification of GA with the acrylic monomer, 3-chloro-2-hydroxypropylmethacrylate (CHPMA). This monomer molecule is known to form biocompatible and chemically stable hydrogels and finds specialized applications in water purification [29]. Grafting of CHPMA onto GA may lead to the development of an efficient adsorbent material fulfilling the requirements of ecofriendly adsorbents for water purification. Due to the presence of carbonyl, chloro and hydroxyl groups, it can greatly enhance the sorption capacity of GA.

In this paper, we report studies on the development of a hybrid hydrogel derived from Gum acacia modified by grafting with poly(3-chloro-2-hydroxypropylmethacrylate) via microwave assisted polymerization process. The hydrogel is further modified by incorporation of magnetite nanoparticles to render it magnetic. The hydrogel and nanocomposite have been studied as an

adsorbent material for absorptive removal of certain dyes and metal ions from their individual aqueous solutions to evaluate its adsorption characteristics in terms of isotherm, kinetic and thermodynamic studies. Finally, the materials were subjected to desorption studies to verify their regenerative efficacy.

2. Experimental

2.1 Materials

Gum acacia (GA), 3-chloro-2-hydroxypropylmethacrylate (CHPMA), iron (III) chloride hexahydrate ($FeCl_3 \cdot 6H_2O$), iron (II) chloride tetrahydrate ($FeCl_2 \cdot 4H_2O$), potassium peroxodisulfate (KPS), ammonium hydroxide (28%), N, N- methylenebisacrylamide (MBA) were received from Aldrich Chemical Company Inc., USA. Methanol was provided by Himedia Laboratories Pvt Ltd., Mumbai, India. Acetone and Hydrochloric acid (HCl) were purchased from S.D. Fine-Chem Ltd., Mumbai, India. Copper sulphate pentahydrate ($CuSO_4.5H_2O$) was supplied by Qualigens Fine Chemicals, Mumbai, India. Mercuric chloride ($HgCl_2$) was provided by Reachem laboratory chemicals Pvt Ltd., Chennai, India. Methylene Blue (MB) was obtained from Rankem Chemicals, Delhi, India. Rhodamine 6G (R6G) was supplied by Loba Chemie Pvt Ltd., Mumbai, India. All chemicals used were devoid of additional purification. For preparing the solutions, double distilled water was chosen.

2.2 Methods

2.2.1 Microwave supported synthesis of Gum acacia-graft-poly(3-chloro-2-hydroxypropylmethacrylate) hydrogel (GA-*g*-PCHPMA)

Microwave assisted synthesis of GA-*g*-PCHPMA hydrogel has been carried out using the free radical polymerization approach. To a solution of 0.2 g of GA in 10 mL distilled water, 2 mL of CHPMA (0.013 mol) was added slowly with uninterrupted stirring followed by 18 mg of KPS (0.066 mmol) and 14.9 mg of MBA (0.097 mmol). The resulting mixture was stirred on a magnetic stirrer thoroughly and the solution was placed in the microwave oven (LG-Gril-Intellowave, India) and irradiated under a power of 80 W for 60 S. The gel obtained was cleansed by washing with acetone, methanol and distilled water frequently and lastly dried in an oven for 24 hrs at 50^o C. The gel sample was designated as GA-*g*-PCHPMA.

2.2.2 Preparation of Gum acacia-graft-poly(3-chloro-2-hydroxypropylmethacrylate)/magnetite nanocomposite (GA-*g*-PCHPMA/Fe_3O_4)

The nanocomposite GA-*g*-PCHPMA/Fe_3O_4 was prepared using the procedure mentioned earlier [13,30].

3. Structural Characterization

Grafting of CHPMA on GA and incorporation of Fe_3O_4 nanoparticles within the polymer matrix of GA-*g*-PCHPMA hydrogel were confirmed by characterization of the gel and the nanocomposite materials as detailed below.

The FTIR spectra of the materials were recorded in the spectral range of 500-4000 cm^{-1} on Fourier transform infrared spectrometer, IR Prestige 21 (Shimadzu, Japan). The surface morphology of the materials was recorded under the acceleration voltage of 5 kV with 4k magnifications using Scanning electron microscope, JEOL-JSM 5800LV (Japan). The X-ray diffraction patterns of the materials were noted at room temperature with an analysis rate 2^o/min over a 2θ range of 0-80^o using the bench top X-ray diffractometer, Rigaku MiniFlex 600 (Japan). Thermal stability of the samples was studied with Thermogravimetric analyser, SDT Q600 V20.9 (Japan). For this study, the samples were heated in the temperature range of 25-700^oC with a heat rating of 10^oC/min under nitrogen atmosphere. By performing nitrogen adsorption-desorption experiments, the Brunauer-Emmet-Teller specific surface area and porosity dimensions were obtained from BELSORP-max, Microtrac BEL (Japan) surface area and porosity analyser. The magnetization value and hysteresis loop of the nanocomposite was measured at room temperature with the help of vibrating sample magnetometer (Model 7410S, Lakeshore Company, USA) having the range -15000 to +15000 O_e in an applied magnetic field of 1.5 T and sensitivity of 10^{-6} emu.

3.1 Adsorption studies

3.1.1 Determination of adsorption capacity and isotherm studies

The adsorption capacities of the hydrogel GA-*g*-PCHPMA and the nanocomposite GA-*g*-PCHPMA/Fe_3O_4 towards R6G, MB, Cu(II) and Hg(II) from their individual aqueous solutions were determined adopting the following procedure.

The aqueous solutions of cationic dyes were prepared in the concentration ranging from 20–1000 mg/L. A known quantity of the dry adsorbent (≈ 0.1 g) was put into 50 mL of adsorbate solution maintained at 30ºC. The residual concentration of the dye in solution was determined by Ultraviolet-Visible spectrophotometer (Shimadzu UV-160A, Japan) after 4 h at the maximum absorption wavelength of MB (663 nm) and R6G (527 nm). The metal ions concentration in solution after adsorption was obtained from atomic absorption spectrophotometer (GBC 932 Plus, Australia). The quantity of dyes and metal ions (mg/g) adsorbed by the adsorbents was calculated using following Eq.

$$q_e = (C_o - C_e) \times \frac{V}{m} \qquad (1)$$

where C_o and C_e indicate the initial and equilibrium concentration of the dye or metal ion (mg/L) in solution respectively, q_e denotes the equilibrium adsorption capacity of the adsorbents (mg/g), V is the volume of aqueous solution (L) taken and m is the mass (g) of the dried adsorbents taken for adsorption experiments.

3.1.2 Kinetics of adsorption

The adsorption of all four adsorbate species was studied as a function of time using 0.1 g samples from a solution of 500 mg/L during 0-4 h period at 30ºC using the procedure mentioned in 3.1.1.

3.1.3. Thermodynamics of adsorption

The effect of temperature on adsorption was studied using 0.1 g samples in 50 mL adsorbate solutions of concentration 500 mg/L at temperatures ranging from 30-50 ºC adopting the procedure mentioned in 3.1.1.

3.2 Desorption studies

Reusability of the hydrogel, GA-*g*-PCHPMA and the nanocomposite GA-*g*-PCHPMA/Fe_3O_4 for the sequestration of dyes and metal ions was planned using the stripping solution of HCl (pH=1.2) by adsorption-desorption experiments. A known weight of the sample (≈ 0.1 g) was suspended in 50 mL of adsorbate solution of concentration 500 mg/L and retained under continuous stirring for 4 h. The adsorbate loaded sample was then taken out, washed, dried and

suspended in stripping solution of pH 1.2 with a constant stirring for 2 h at room temperature. The quantity of adsorbates desorbed into the acid solution was analyzed as per the method in section 3.1.1. The percentage of desorption (%D) was obtained using the Eq.,

$$\%D = \frac{\text{Amount of dye/metal ions desorbed}}{\text{Amount of dye/metal ions adsorbed}} \times 100 \qquad (2)$$

4. Results and discussion

4.1 Formation of GA-*g*-PCHPMA/Fe_3O_4 nanocomposite

The synthetic procedure adopted for the preparation of the gel and the nanocomposite samples is presented in Scheme 1. The sulphate anion radicals formed from KPS on microwave irradiation displace hydrogen atom from hydroxyl groups of gum acacia to generate GA macro-radicals ($GA-O^{\cdot}$). The $GA-O^{\cdot}$ radicals attack the monomer, CHPMA initiating the formation of graft polymer chain on the GA backbone. Incorporation of MBA, a tetrafunctional monomer in the graft polymer chain leads to the formation of a 3D structure. The loading of the Fe^{2+} and Fe^{3+} ions in the hydrogel could be monitored visually by the color variation of the swollen hydrogel from colourless to yellow–orange. The intensity of colour in the hydrogel is influenced by the iron concentration of the solution which remained even after repeated washing of the gel with water, signifying that the Fe ions are strongly bound to the gel matrix. On suspending this sample in NH_4OH solution, a quick color change was detected from yellow–orange to black, indicating spontaneous generation of magnetite nanoparticles in the hydrogel network. The reactions leading to the formation of Fe_3O_4 nanoparticles during in-situ generation are given below [31].

$Fe^{3+} + 3OH^- \rightarrow Fe(OH)_3$

$Fe(OH)_3 \rightarrow FeOOH + H_2O$

$Fe^{2+} + 2OH^- \rightarrow Fe(OH)_2$

$2FeOOH + Fe(OH)_2 \rightarrow Fe_3O_4 + 2H_2O$

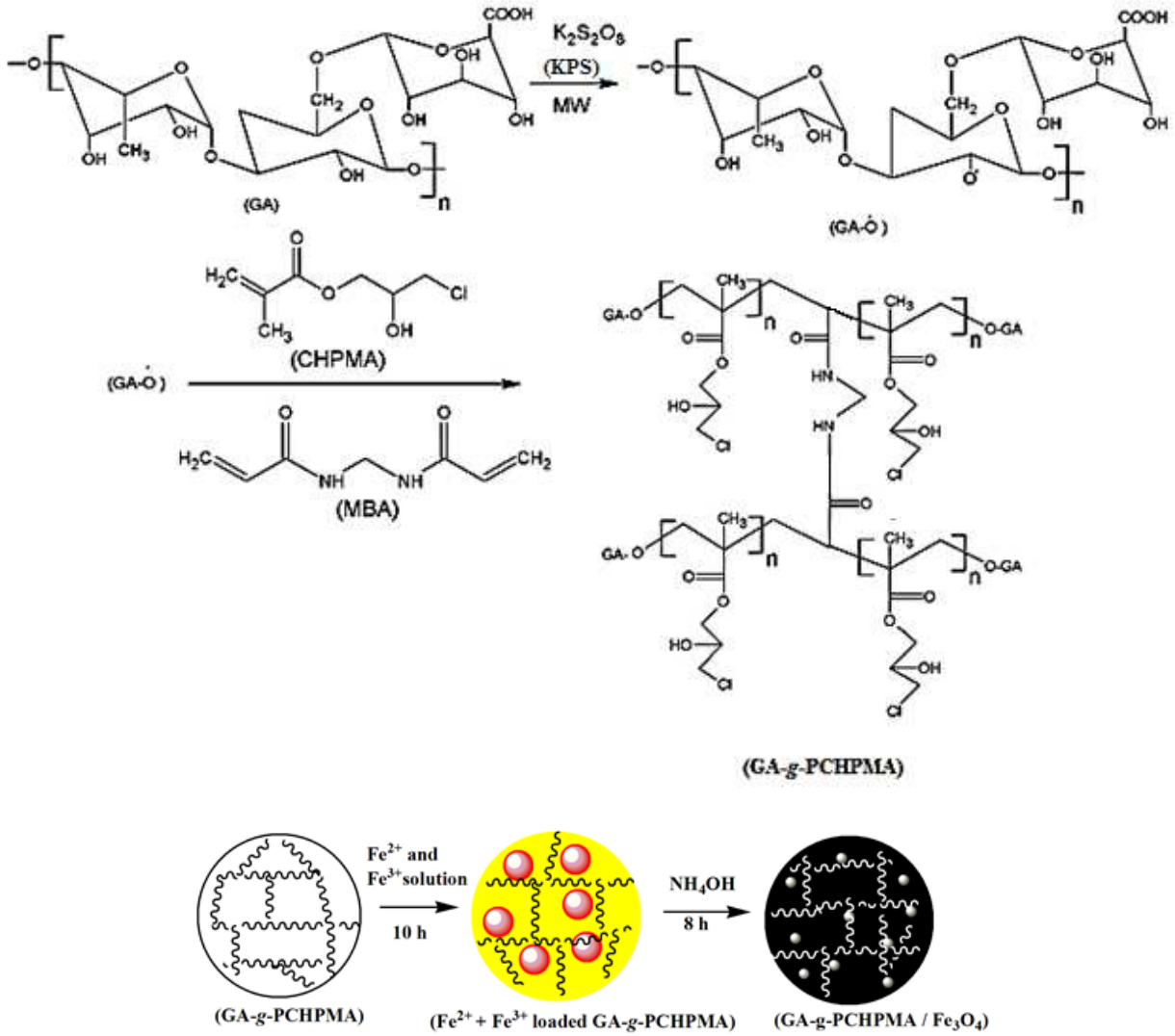

Scheme 1: Formation of GA-*g*-PCHPMA/Fe_3O_4 nanocomposite

4.2 Infrared spectral characterization

FTIR was used to confirm the modification of GA with CHPMA and incorporation of Fe_3O_4 nanoparticles. The spectra of the grafted gel and the nanocomposite are displayed in Fig 1b and c respectively. The spectrum of GA is given in Fig. 1a for comparison. The broad band which appeared at 3381 cm^{-1} in all three spectra is attributed to the O-H stretching of hydroxyl groups. The band detected at 2942 cm^{-1} indicated C–H stretching of GA. The symmetric stretching and asymmetric stretching vibrations of –COOH group was observed at 1612 and 1409 cm^{-1}. The band corresponding to glycosidic linkage of GA appeared at 1026 cm^{-1}. In the IR spectra of GA-*g*-PCHPMA (Fig. 1b) a sharp and prominent band related to the C=O stretching vibration from

ester linkage of CHPMA units can be seen at 1703 cm^{-1}. The band at 1444 cm^{-1} is due to bending vibrations of methylene group, whereas bands at 1251 and 1151 cm^{-1} are due to C–O stretching vibrational modes of the ester linkages and alcoholic groups on GA respectively. Moderately low intensity band at 746 cm^{-1} can be assigned to the C-Cl stretching vibration. The new band appearing in the spectrum of GA-*g*-PCHPMA/Fe_3O_4 (Fig. 1c) at 553 cm^{-1} is attributed to Fe–O, indicative of the entrapment of magnetite nanoparticles within the gel matrix.

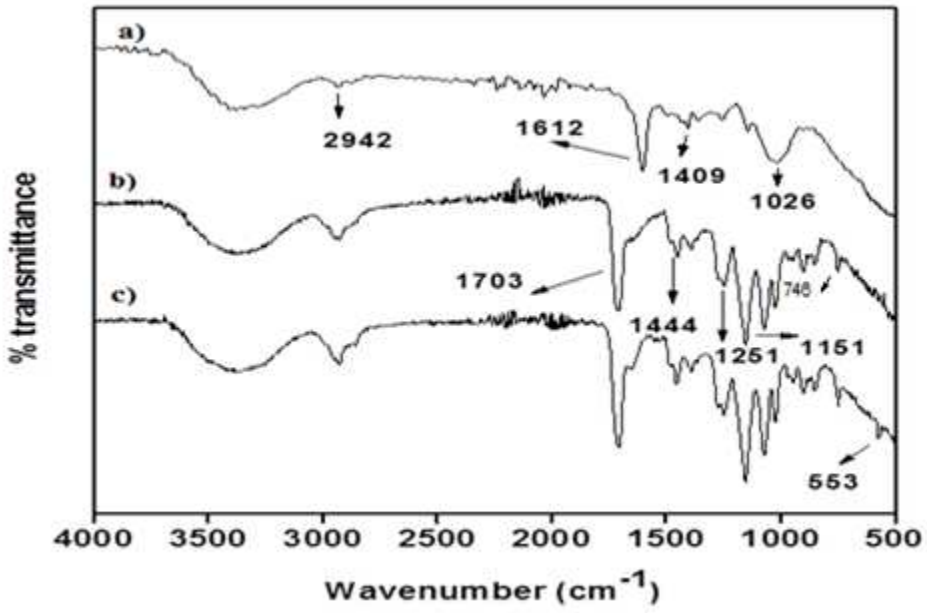

Fig. 1: FTIR spectra of a) GA b) GA-*g*-PCHPMA c) GA-*g*-PCHPMA/Fe_3O_4

4.3 SEM analysis

FESEM image of GA-*g*-PCHPMA (Fig 2a) shows a flake like rough surface. The roughness of the surface is highly appropriate for the sorption applications. The morphology of the GA-*g*-PCHPMA/Fe_3O_4, as seen in the Fig. 2b, appears to have a homogeneous distribution of spherical magnetite nanoparticles without noticeable agglomeration. The presence of voids in between the nanoparticles makes the surface more attractive for adsorption process. The results showed that the magnetite nanoparticles have the average particle size of 10-19 nm.

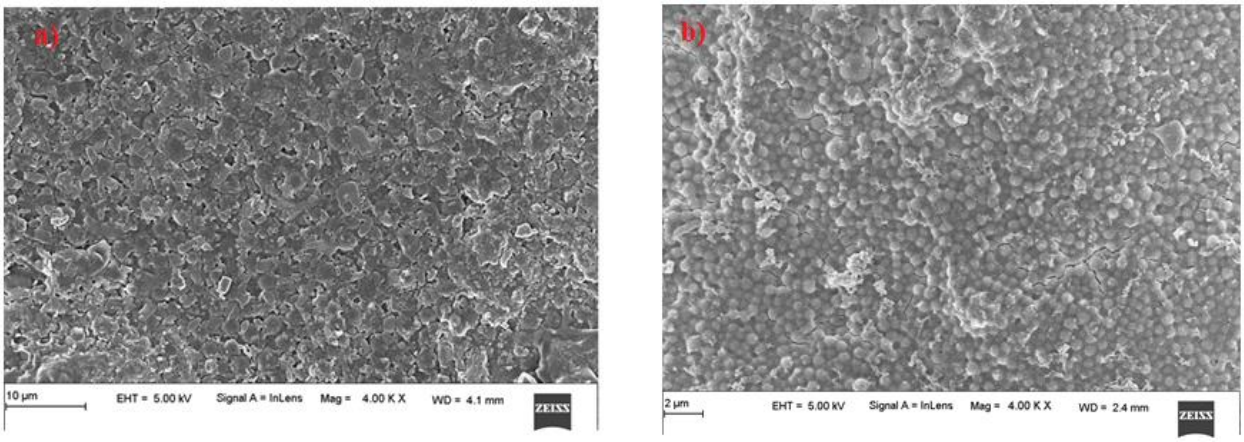

Fig. 2: SEM images of a) GA-*g*-PCHPMA b) GA-*g*-PCHPMA/Fe_3O_4

4.4 XRD analysis

XRD is intensively employed as an efficient technique to examine the crystallinity of the material. The XRD patterns of GA-*g*-PCHPMA and GA-*g*-PCHPMA/Fe_3O_4 are displayed in Fig. 3a and b respectively. As presented in Fig. 3a, GA-*g*-PCHPMA exhibits a diffraction peak centered on $2\theta = 20.1°$, which was typical impression of semicrystalline nature of the hydrogel. However, in the case of GA-*g*-PCHPMA/Fe_3O_4 (Fig. 3b), few sharp peaks are observed at 2θ = 23.2, 30.8, 35.2, 53.9, 57.2° which establishes the uniform dispersion of a low amount of crystalline magnetite nanoparticles in the composite network. These characteristic peaks are corresponding to the planes (111), (220), (311), (422), (511) obtained from XRD data are consistent with the JCPDS (82-1533) data of magnetite nanoparticles. The only notable change is the fall in peak intensities due to the incorporation of Fe_3O_4 nanoparticles. The result also reveals enhanced crystallinity of the gel on nanocomposite formation.

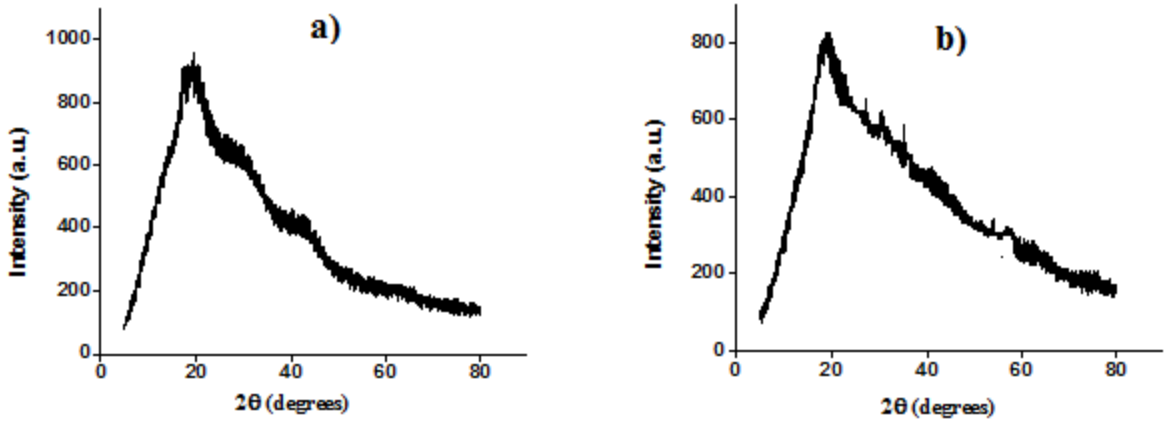

Fig. 3: XRD patterns of a) GA-*g*-PCHPMA b) GA-*g*-PCHPMA/Fe_3O_4

4.5 TGA analysis

The fabricated materials were subjected to thermogravimetric analysis to study their thermal stability and the results are depicted in Fig. 4. As shown in Fig. 4a, the exclusion of hydrogen bonded water leads to a small weight loss of 15% as the GA is heated from 25-107°C. The most significant weight loss of 52% occurred in the region 230-358°C which is credited to the structural breakdown of the polysaccharide chain. When the temperature was increased to 610°C, weight loss of 28% was observed due to complete loss of degraded sample. As seen from Fig. 4b, GA-*g*-PCHPMA experienced an initial weight loss of 8% followed by 83% loss in the second stage in the temperature range 253-437°C. On heating beyond this temperature an additional weight loss 9% was seen owing to degradation of grafted side chains and the decomposed polysaccharide components. As observed from Fig. 4c, the degradation of the nanocomposite sample appears to be very similar to the parent graft copolymer gel during the first two stages. Beyond 450°C, no further weight loss is observed and a mass 12% remains undegraded owing to the presence of magnetite nanoparticles. The thermogravimetric analysis thus gives evidence for the incorporation of metal particles into the hydrogel rendering it an inorganic-organic hybrid material.

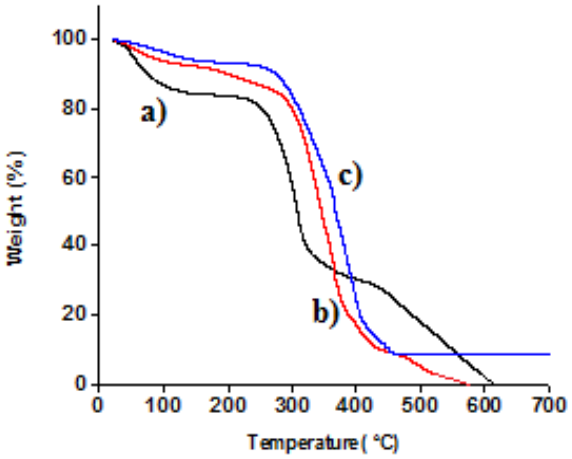

Fig. 4: TGA curves of a) GA b) GA-*g*-PCHPMA c) GA-*g*-PCHPMA/Fe_3O_4

4.6 Brunauer-Emmett-Teller (BET) surface area analysis

The interior variations in physical structure of the gel and the nanocomposite samples were observed by BET studies. The BET plots are displayed in supporting information (Fig S1). The surface area, pore diameter and pore volume obtained for hydrogel GA-*g*-PCHPMA were 0.481 m^2g^{-1}, 3.0556 nm and 0.016 cm^3g^{-1} respectively. The nanocomposite GA-*g*-PCHPMA/Fe_3O_4 displayed a much larger surface area of 2.524 m^2g^{-1} but pore diameter remained almost similar (3.0578 nm). Moreover, the pore volume increases almost 3 times (0.043 cm^3g^{-1}) on formation of the nanocomposite. The pore sizes of the hydrogel and the nanocomposite are similar to mesoporous materials according to IUPAC standard [32]. The appreciable expansion in pore volume and surface area of the hybrid nanomaterial is due to the influence of Fe_3O_4 nanoparticles which provides channels for adsorption of adsorbate species and makes them to settle into the pores. A related observation has been reported in earlier studies [5,33,34].

4.7 Magnetic property measurement

The variation of the magnetization with applied magnetic field brings evidence of the magnetic properties of the nanocomposite and is displayed in Fig. 5. The magnetization curve reveals that the residual magnetization (remanence) and coercive force (coercivity) were found to be zero. The saturation magnetization (M_s) value observed was 0.15 emu g^{-1} at room temperature. This value is much lower than the value observed for pure magnetite nanoparticles (66.1 emu g^{-1}) [30], which might be due to the low amount of magnetite nanoparticles in the nanocomposite. Further, it has been reported that M_s value tends to reduce when magnetite nanoparticles are embedded in non-magnetic materials [35]. The magnetization curve also recommended the superparamagnetic nature of GA-*g*-PCHPMA/Fe_3O_4. The magnetic nature makes it a very useful material in applications like removal of pollutants from contaminated water samples [36].

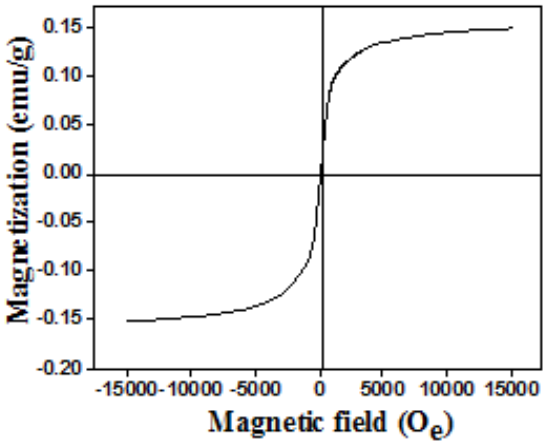

Fig. 5: Magnetization curve of GA-*g*-PCHPMA/Fe_3O_4 at room temperature

4.8 Adsorption studies

4.8.1 Effect of initial dye/metal ion concentration

The initial concentration of the adsorbate species has a significant influence on the amount adsorbed by the adsorbent samples. It provides essential driving force to conquer the resistance to mass transfer between the solid and aqueous phase. The results shown in Fig. 6 indicate that a linear growth of q_e with increase in concentrations of the dyes and metal ions in solution from zero to 800 mg/L while no change was observed beyond 800 mg/L. Increase in q_e can be attributed to the large concentration gradient of the dyes and metal ions around the vicinity of the adsorption spots. However, the attainment of equilibrium can be due to the non-availability of adequate adsorption spots on the adsorbent to accommodate a large number of adsorbate species. The adsorbates were adsorbed to different extent on the gel and the nanocomposite, the order being R6G>Cu(II)>Hg(II)>MB in both cases.

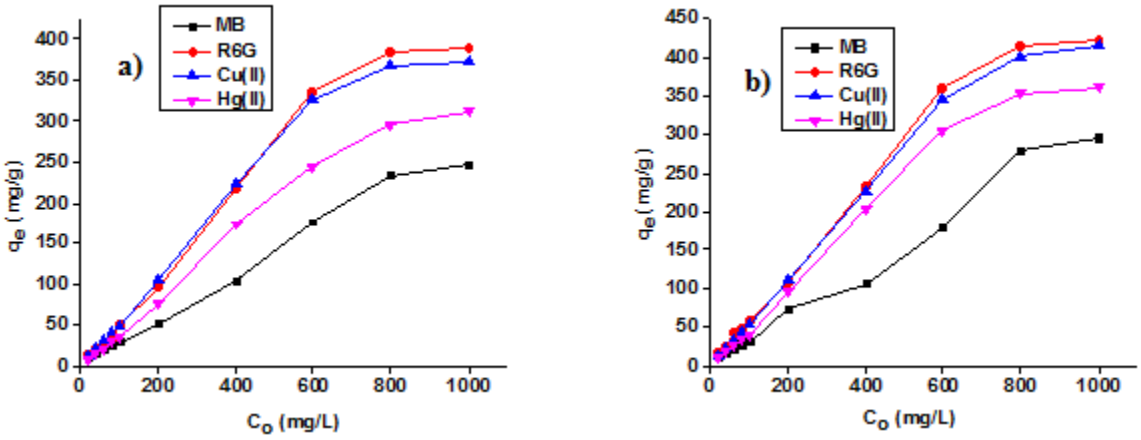

Fig. 6: The effect of initial concentration of dyes and metal ions on adsorption for a) GA-*g*-PCHPMA b) GA-*g*-PCHPMA/Fe_3O_4 (t = 4 hrs, T =30^{o}C)

4.8.2 Effect of contact time

Fig. 7 presents the effect of contact time on the extent of adsorption of the hydrogel and the nanocomposite from a solution of 500 mg/L concentration. Higher uptake was observed initially for both the adsorbents due to the presence of a sufficiently superior quantity of adsorption sites. Complete saturation of the adsorption sites occurred after a contact time of 120 min for MB, R6G and 45 min for Cu(II), Hg(II). No significant uptake of the dyes and metal ions was observed beyond this time indicating the attainment of equilibrium state. It was detected that the adsorption of metal ions was much rapid at the early stage when compared to dyes. Also it is apparent from the figure that the adsorption of R6G and Cu(II) is the highest when matched to MB and Hg(II) on both the adsorbents. The impact of magnetite nanoparticles on adsorption process is significant from the enhanced adsorption capacity of GA-*g*-PCHPMA/Fe_3O_4 over GA-*g*-PCHPMA.

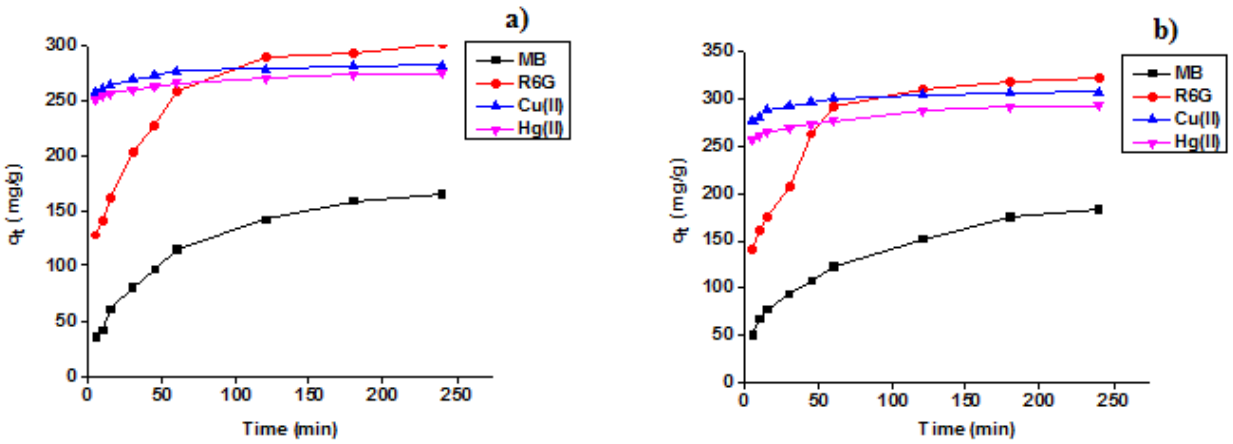

Fig. 7: The effect of contact time on the adsorption of dyes and metal ions on a) GA-*g*-PCHPMA b) GA-*g*-PCHPMA/Fe_3O_4 (C_o = 500 mg/L, T =30°C)

4.8.3 Mechanism of adsorption

The possible mechanism for adsorption of cationic dyes (MB and R6G) on the materials is presented in Fig. S2. Under neutral pH conditions, GA acts as an anionic polysaccharide and the electrostatic interaction operating between the $–COO^-$ groups on hydrogel and the cationic dye has the crucial role for the adsorption process. Adsorption is also driven by the availability of polar functional groups on the hydrogel such as -CONH-, -OH and $-CH_2Cl$ which are involved in dipole-dipole and H-bonding interactions with cationic dye molecules [24]. The possible mechanism for adsorption of bivalent metal ions (Cu^{2+} and Hg^{2+}) on the materials is shown in Fig. S3. The foremost interactive sites for the adsorption of metal ions are the carboxyl, chloro, amide and hydroxyl groups of the hydrogel. As the chloro group; nitrogen and oxygen atoms of the amide group; and the oxygen atoms of carboxyl group have lone pair of electrons, the metal ions are bound to the gel by coordinate bonds [26]. The adsorption of dyes and metal ions is also influenced by the large pore size and surface area of the adsorbents. Introduction of magnetite nanoparticles into the gel matrix increased the surface area and brought large porosity (as deliberated in section 4.6) which enhances the adsorption efficiency of the parent gel [37].

4.8.4 Adsorption isotherm models

The adsorption isotherm explains the dispersal of dye molecules and metal ions between the liquid and the solid phase, when the processes involved is in equilibrium. To reveal the interactive performance between the adsorbent and adsorbate species, two adsorption isotherm

models, namely Langmuir [38] and Freundlich [39] models were used to fit the adsorption data obtained in the present study.

Langmuir isotherm can be represented as follows:

$$\frac{C_e}{q_e} = \frac{1}{q_m} C_e + \frac{1}{q_m K_L} \qquad (3)$$

where C_e (mgL^{-1}) is the equilibrium concentration of adsorbates, q_e (mgg^{-1}) is the equilibrium adsorption capacity of adsorbates, q_m (mgg^{-1}) is the theoretical saturation adsorption capability for monolayer coverage and K_L is the Langmuir constant related to the attraction of binding spots and is a measure of the adsorption energy. These constants can be obtained from the slope and intercept of the linear plot of C_e/q_e versus C_e. In addition, the parameter R_L is obtained from Eq. (4) to identify feasibility of an adsorption isotherm.

$$R_L = \frac{1}{1 + K_L C_0} \qquad (4)$$

where, C_o (mgL^{-1}) is the highest initial concentration of adsorbent conforming to maximum adsorption. If $R_L = 1$, then adsorption is linear; if $R_L > 1$, then adsorption is unfavorable; if $R_L = 0$, then the adsorption is irreversible and if $0 < R_L < 1$, the adsorption is favorable.

Freundlich adsorption isotherm is appropriate for heterogeneous adsorbent surface and solutions of low concentration of adsorbate. Mathematical form for Freundlich model is represented as:

$$\log q_e = \frac{1}{n} \log C_e + \log K_F \qquad (5)$$

where, q_e and C_e have their importance as stated before. The Freundlich isotherm constants, n and K_F are associated to the adsorption intensity and the adsorption capability of the material respectively. Their values are obtained from the slope and intercept of the linear plot between log q_e and log C_e respectively. The values of 'n' varying from 1-10 support the promising situation for adsorption.

The Fig. S4 and Fig. 8 represents Langmuir and Freundlich isotherm fit adsorption data for the diverse adsorbate species used in the present study respectively. The values of various parameters of Langmuir and Freundlich isotherm model are given in Table 1. It is evident from

Fig. 8 that the Freundlich isotherm model shows a better fit with the experimental data in comparison to the Langmuir isotherm model. Also the higher R^2 values for the Freundlich isotherm fit indicates the best fit of Freundlich model. The heterogeneity factor 'n' in Freundlich isotherm was greater than unity, which suggested that the adsorption of all planned adsorbates on both the samples is favorable in the whole range of concentrations considered for adsorbate species. From the results it is proven that adsorption of dyes and metal ions on both the materials implicate the multilayer adsorption process and are found to be heterogeneous in nature.

Isotherm model	Parameters	Adsorbate							
		MB		R6G		Cu(II)		Hg(II)	
		GA-*g*-PCHPMA	GA-*g*-PCHPMA/Fe_3O_4	GA-*g*-PCHPMA	GA-*g*-PCHPMA/Fe_3O_4	GA-*g*-PCHPMA	GA-*g*-PCHPMA/Fe_3O_4	GA-*g*-PCHPMA	GA-*g*-PCHPMA/Fe_3O_4
Freundlich	K_F	1.17	1.56	2.02	5.48	6.28	10.02	1.03	2.72
	n	1.21	1.24	1.17	1.41	1.28	1.36	1.02	1.14
	R^2	0.96	0.94	0.95	0.97	0.91	0.92	0.97	0.91
Langmuir	R_L	0.59	0.62	0.35	0.17	0.12	0.07	0.58	0.31
	$K_L(\times10^3)$	0.67	0.59	1.81	4.82	7.57	12.8	0.71	2.31
	q_m (mgg^{-1})	843.3	1111.1	714.2	526.3	555.6	520.6	1428.5	833.4
	R^2	0.21	0.12	0.47	0.84	0.83	0.89	0.23	0.34

Table 1: Isotherm parameters for the adsorption of dyes and metal ions on GA–*g*–PCHPMA and GA–*g*–PCHPMA/Fe_3O_4

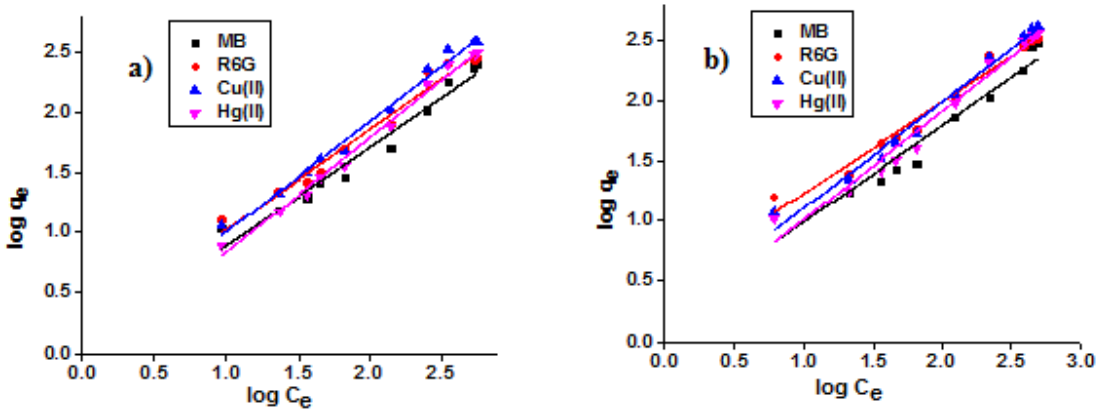

Fig. 8: Freundlich isotherm model fit for the adsorption of dyes and metal ions on a) GA–*g*–PCHPMA and b) GA–*g*–PCHPMA/Fe_3O_4

4.8.5 Kinetics of adsorption

The rate of dye and metal ion uptake is governed by the contact time of the solid adsorbent with the adsorbate solution. As the adsorption process begins, the adsorbate species relocate from solution to the external superfice of the adsorbent, forspread in the frontier layer and eventually migrate from the superfice into the interior sites by way of pore diffusion. Thus, to explore the adsorption kinetics and understand the mechanism of adsorption, data were fitted into pseudo-first-order and pseudo-second-order kinetic models [40, 41].

Integrated mathematical forms of pseudo first order and pseudo second order rate expressions are denoted by equations (6) and (7) respectively.

$$\log(q_e - q_t) = \log q_e - \frac{k_1 t}{2.303} \qquad (6)$$

$$\frac{t}{q_t} = \frac{1}{k_2 q_e^2} + \frac{t}{q_e} \qquad (7)$$

where q_e (mg g^{-1}) and q_t (mg g^{-1}) are amount of adsorbate species adsorbed per unit mass of adsorbent at equilibrium and at time t respectively, k_1 (min^{-1}) is pseudo first order adsorption rate constant and k_2 (g mg^{-1} min^{-1}) is pseudo second order adsorption rate constant. The slope of plots between '$\log (q_e-q_t)$ vs t' and 't/q_t vs t', give the values of k_1 and k_2 respectively.

The Fig. S5 and Fig. 9 represent kinetic adsorption plots of GA-*g*-PCHPMA and GA-*g*-PCHPMA/Fe_3O_4 on four different adsorbate species. Values of various constants obtained using these two models along with R^2 values are given in Table 2. Values of q_e calculated using pseudo second order rate equation was found to match well with the experimental value, which suggests the suitability of pseudo second order kinetic model to describe the adsorption of dyes and metal ions onto GA-*g*-PCHPMA and GA-*g*-PCHPMA/Fe_3O_4. The best fit of pseudo second order model is further confirmed by the R^2 values close to unity in this model fit. This point out that chemisorption as the rate governing mechanism for adsorption.

	Adsorbate							
	MB		R6G		Cu(II)		Hg(II)	
	GA-*g*-PCHPMA	GA-*g*-PCHPMA /Fe_3O_4	GA-*g*-PCHPMA	GA-*g*-PCHPMA /Fe_3O_4	GA-*g*-PCHPMA	GA-*g*-PCHPMA /Fe_3O_4	GA-*g*-PCHPMA	GA-*g*-PCHPMA /Fe_3O_4
q_e (exp) (mg g^{-1})	224.4	265.2	283.5	344.4	282.4	307.5	275.3	292.8
Kinetic model								
Pseudo first order								
q_e (mg g^{-1})	193.1	235.1	147.2	177.7	21.8	26.6	24.9	41.4
k_1 ($\times 10^3$) (min^{-1})	7.1	7.2	8.7	7.8	17.1	18.1	16.3	19.1
R^2	0.94	0.89	0.94	0.97	0.96	0.98	0.98	0.98
Pseudo second order								
q_e (mgg^{-1})	243.9	285.3	285.7	344.8	285.5	312.5	240.0	294.1
k_2 ($\times 10^5$) ($gmg^{-1}min^{-1}$)	6.7	5.5	19.4	15.2	298.8	249.8	277.7	152.1
R^2	0.97	0.95	0.99	0.99	1.00	1.00	0.99	0.99

C_o = 500 mgL^{-1}, T = 30°C

Table 2: Kinetic parameters for the adsorption of dyes and metal ions on GA–*g*–PCHPMA and GA–*g*–PCHPMA/Fe_3O_4

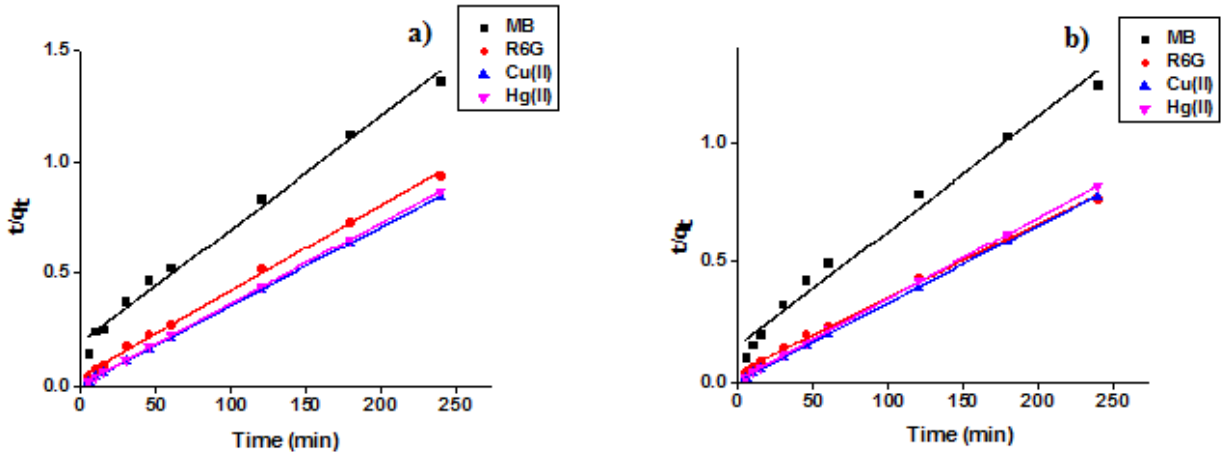

Fig. 9: Pseudo second order kinetic plot for adsorption of dyes and metal ions on a) GA–*g*–PCHPMA b) GA–*g*–PCHPMA/Fe_3O_4

The GA–*g*–PCHPMA/Fe_3O_4 exhibited higher adsorption capacity for all the studied adsorbate species in comparison to GA–*g*–PCHPMA. The maximum adsorption capacity of the GA–*g*–PCHPMA towards MB, R6G, Cu(II) and Hg(II) were found to be 224.4, 283.5, 282.4 and 275.3 mg g^{-1} respectively and the corresponding values for GA–*g*–PCHPMA/Fe_3O_4 are 265.2, 344.4, 307.5 and 292.8 mg g^{-1} respectively. The enhanced adsorption ability of the GA–*g*–PCHPMA/Fe_3O_4 could be ascribed to increased surface area and porosity of the nanocomposite owing to the embedded Fe_3O_4 nanoparticles. The adsorption was higher in the case of R6G compared to MB. Despite their large size, R6G dye molecules are adsorbed to higher extent than the MB molecules which could be due to the greater number of binding spots on the former compared to the latter. This phenomenon could be accompanying with the higher solubility of MB (43.6 gL^{-1}) compared to R6G (20 gL^{-1}). On the basis of solubility of substances, it has been established that substances more soluble in water are temperately less easily adsorbed than substances with reduced solubility [42]. The results also indicated that the extent of adsorption was lower for Hg^{2+} compared to Cu^{2+}. The larger ionic radius and a smaller charge density of Hg^{2+} ion (102 pm and 49 coulomb/mm^3) compared to Cu^{2+} ion (73 pm and 116 coulomb/mm^3) greatly influenced the adsorption on both adsorbents. This evidently specifies that the formation of more stable complexes takes place due to interaction of lone pair of electrons on the nitrogen and oxygen atoms of the gel with Cu^{2+} ions compared with Hg^{2+} ions [43].

4.8.6 Thermodynamics of adsorption

To understand the feasibility of adsorption and to understand the thermodynamic aspects of adsorption on GA–*g*–PCHPMA and GA–*g*–PCHPMA/Fe_3O_4, van't Hoff equations were applied.

$$\ln K_C = -\frac{\Delta H^0}{R}\frac{1}{T} + \frac{\Delta S^0}{R} \qquad (8)$$

The ratio of q_e and C_e gives the value of the equilibrium constant of adsorption, K_C. Where, T is temperature (K) and R is gas constant (8.314 $Jmol^{-1}K^{-1}$). The Fig. 10 shows the linear plot of ln K_C vs 1/T. The intercept and slope obtained from this plot gives the values of standard entropy change (ΔS°) and standard enthalpy change of adsorption (ΔH°) respectively. Using the ΔH° and ΔS° values; the standard free energy change, ΔG° was calculated using the Eq.,

$$\Delta G^o = \Delta H^o - T\Delta S^o \qquad (9)$$

The obtained values of the thermodynamic parameters are displayed in Table 3.

The negative values of ΔG^o revealed the spontaneous nature of adsorption of dyes and metal ions on both the adsorbents. Also, the decrease in the magnitude of ΔG^o with temperature suggested that the adsorption is favourable at low temperature. The negative values of ΔH^o for all the studied adsorbates indicated the exothermic nature of the process. In addition, the negative value of ΔS^o corresponded to decrease in the degree of freedom of the adsorbed dyes and metal ions on the adsorbents.

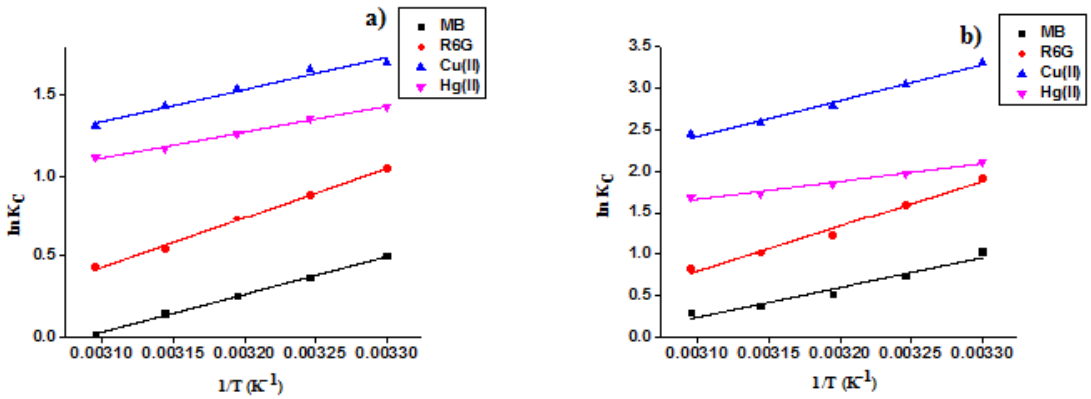

Fig. 10: Plot of ln K_C versus 1/T for the uptake of dyes and metal ions on a) GA–*g*–PCHPMA and b) GA–*g*–PCHPMA/Fe_3O_4

Adsorbent	Adsorbate	$-\Delta H^o$ (kJ mol^{-1})	$-\Delta S^o$ (kJ $mol^{-1}K^{-1}$)	$-\Delta G^o$ (kJ mol^{-1})				
				303 K	308 K	313 K	318 K	323 K
	MB	19.39	0.05	1.24	0.92	0.64	0.36	0.02
GA-*g*-	R6G	25.84	0.07	2.64	2.24	1.91	1.42	1.14
PCHPMA	Cu(II)	16.51	0.04	4.28	4.24	3.99	3.77	3.51
	Hg(II)	13.32	0.03	3.59	3.47	3.28	3.09	2.98
	MB	29.82	0.09	2.54	1.85	1.31	0.93	0.74
GA-*g*-	R6G	45.66	0.13	4.83	4.08	3.17	2.65	2.18
PCHPMA/	Cu(II)	35.84	0.09	8.31	7.81	7.27	6.81	6.55
Fe_3O_4	Hg(II)	17.82	0.04	5.31	5.07	4.81	4.59	4.51

Table 3: Thermodynamic parameters for the adsorption of dyes and metal ions on GA–*g*–PCHPMA and GA–*g*–PCHPMA/Fe_3O_4

4.8.7 Desorption study

The desorption efficiency and regeneration power of GA–*g*–PCHPMA and GA–*g*–PCHPMA/Fe_3O_4 were studied in acidic solution of pH 1.2. Fig. 11 shows the desorption capacities of both the adsorbents for studied adsorbates over one adsorption–desorption cycle. The results indicate that the desorption capacities of GA–*g*–PCHPMA for MB, R6G, Cu(II) and Hg(II) are 91.3, 89.9, 83.1 and 82.9% respectively. This observation is presumably inferable to availability of H^+ ions in solution, ensuring in an increased driving force for ion-exchange, facilitating the desorption process. The nanocomposite GA–*g*–PCHPMA/Fe_3O_4 exhibited higher desorption percentage, the corresponding values being 95.6, 93.8, 89.7 and 86.4% respectively. The desorption study confirms the possibility of recovery of adsorbate species and reuse of the adsorbent effectively. Thus, it can be stated, based on the results of this study that GA–*g*–PCHPMA/Fe_3O_4 may find potential applications as a high-performance, inexpensive, recyclable adsorbent for wastewater remediation.

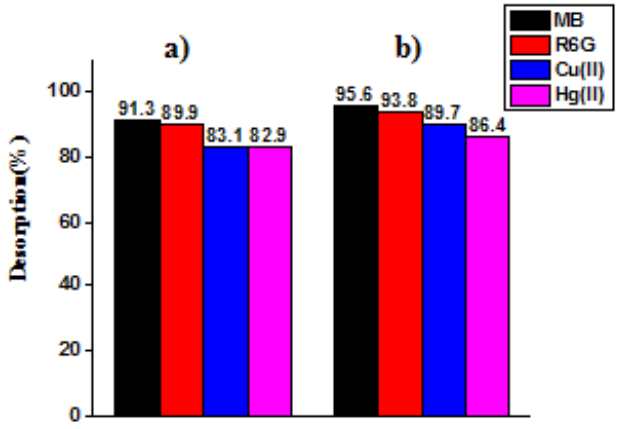

Fig. 11: Desorption (%) of dyes and metal ions from a) GA–*g*–PCHPMA and b) GA–*g*–PCHPMA/Fe_3O_4

4.8.8 Comparison study

The adsorption capability of the GA–*g*–PCHPMA/Fe_3O_4 is matched with other developed gum acacia adsorbent materials reported in literature. The isotherm and kinetic models applicable for adsorption on these materials have also been provided. The comparison data is presented in Table 4 shows good efficacy of GA–*g*–PCHPMA/Fe_3O_4 to remove the studied adsorbates compared to many other reported materials.

Adsorbent	Dye/Metal	q_e (mg/g)	Isotherm model	Kinetic model	Reference
Gum arabic-*g*-polyacrylamide/ZnO	Malachite green	766.5	Langmuir	Pseudo second order	[44]
Gum arabic-*g*-polyacrylamide	Crystal violet	90.9	Langmuir	Pseudo first order	[24]
Gum arabic-Magnetic nanoparticle	Cu(II)	38.5	Langmuir	-	[45]
Gum arabic-*g*-polyacrylonitrile	Pb(II)	1017.0	Langmuir	Pseudo second order	[26]
	Cd(II)	413.0			
	Cu(II)	396.0			

Gum arabic-*g*-polyacrylamide/SiO_2	Eu	5.7	Langmuir	Pseudo first order	[46]
	La	5.6			
	Nd	7.3			
	Sc	5.1	Freundlich		
Gum acacia-*g*-poly(3-chloro-2-hydroxypropylmethacrylate)/Fe_3O_4	MB	265.2	Freundlich	Pseudo second order	Present study
	R6G	344.4			
	Cu(II)	307.5			
	Hg(II)	292.8			

Table 4: Comparison of the adsorption capacity, isotherm and kinetic model fit of present system with other reported systems.

5. Conclusion

A novel biopolymer based adsorbent GA–*g*–PCHPMA has been developed by graft copolymerization of GA with the acrylic monomer CHPMA and converting it into a nanocomposite material GA–*g*–PCHPMA/Fe_3O_4, by incorporation of nano-sized magnetite particles. The FTIR, SEM, XRD, TGA, BET and VSM studies evidenced the incorporation of magnetite nanoparticles within hydrogel matrix. Cationic dyes and metal ions uptake ability of the materials was studied using MB, R6G, Cu(II), Hg(II) under varying conditions and isotherm, kinetic, thermodynamic parameters were established. As compared to the parent gel, the magnetic nanocomposite exhibited extremely high adsorption efficiency towards these adsorbate species. The preferred order of adsorption was R6G > MB and Cu(II) > Hg(II). The adsorption of dyes and metal ions on both the adsorbents was found to follow Freundlich isotherm model and well explained by pseudo second order kinetic model. The thermodynamic analysis manifested the fact that adsorption is exothermic and spontaneous. Meanwhile excellent regeneration of the adsorbents and recovery of the adsorbed species indicated its promising reuse for water purification. The nanocomposite possessed super-paramagnetic nature, thermal stability, high surface area and porous structure which make it a unique material for potential applications in wastewater treatment.

References

[1] Arun Krishna K, Vishalakshi B (2017) Gellan gum-based novel composite hydrogel: evaluation as adsorbent for cationic dyes. J. Appl. 134: 45527. https://doi.org/10.1002/app.45527.

[2] Rajabi M, K. Mahanpoor, Moradi O (2017) Removal of dye molecules from aqueous solution by carbon nanotubes and carbon nanotube functional groups: critical review. RSC Adv. 7: 47083–47090. https://doi.org/10.1039/C7RA09377B.

[3] Han X, Yuan J, Ma X (2014) Adsorption of malachite green from aqueous solutions onto lotus leaf: equilibrium, kinetic, and thermodynamic studies. Desalin. Water Treat. 52: 5563–5574. https://doi.org/10.1080/19443994.2013.813102.

[4] Dragan ES, Loghin DFA (2018) Fabrication and characterization of composite cryobeads based on chitosan and starches-*g*-PAN as efficient and reusable biosorbents for removal of Cu^{2+}, Ni^{2+} and Co^{2+} ions. Int. J. Biol. Macromol. 120: 1872–1883. https://doi.org/10.1016/j.ijbiomac.2018.10.007.

[5] Sun S, Zhu L, Liu X, Wu L, Dai K, Liu C, Shen C, Guo X, Zheng G, Guo Z (2018) Superhydrophobic shish-kebab membrane with self-cleaning and oil/water separation properties. ACS Sustain. Chem. Eng. 6: 9866–9875. https://doi.org/10.1021/acssuschemeng.8b01047.

[6] Gong K, Hu Q, Yao L, Li M, Sun D, Shao Q, Qiu B, Guo Z (2018) Ultrasonic pretreated sludge derived stable magnetic active carbon for Cr(VI) removal from wastewater. ACS Sustain. Chem. Eng. 6: 7283–7291. https://doi.org/10.1021/acssuschemeng.7b04421.

[7] Chen J, Wang X, Huang Y, Lv S, Cao X, Yun J, Cao D (2018) Adsorption removal of pollutant dyes in wastewater by nitrogen-doped porous carbons derived from natural leaves. Eng. Sci. 5: 30–38. https://doi.org/10.30919/es8d666.

[8] Qi X, Liu R, Chen M, Li Z, Qin T, Qian Y, Zhao S, Liu M, Zeng Q, Shen J (2019) Removal of copper ions from water using polysaccharide-constructed hydrogels. Carbohydr. Polym. 209: 101–110. https://doi.org/10.1016/j.carbpol.2019.01.015.

[9] Su T, Wu L, Pan X, Zhang C, Shi M, Gao R, Qi X, Dong W (2019) Pullulan-derived nanocomposite hydrogels for wastewater remediation: synthesis and characterization. J. Colloid Interf. Sci. 542: 253–262. https://doi.org/10.1016/j.jcis.2019.02.025.

[10] Hamza MF, Wei Y, Mira HI, Abdel-Rahman AAH, Guibal E (2019) Synthesis and adsorption characteristics of grafted hydrazinyl amine magnetite-chitosan for Ni(II) and Pb(II) recovery. Chem. Eng. J. 362: 310–324. https://doi.org/10.1016/j.cej.2018.11.225.

[11] Sirajo AZ, Vishalakshi B (2018) Absorptive removal of Cu^{2+} and Pb^{2+} from aqueous solutions using xanthan gum-g-poly[(N,N′-dimethylacrylamide)-co-(2-acrylamido-2-methylpropanesulfonic acid)]–ZnO nanocomposite gel. Sep. Sci. Technol. 54: 2164-2179. https://doi.org/10.1080/01496395.2018.1541094.

[12] Mittal H, Parashar V, Mishra S, Mishra A (2014) Fe_3O_4 MNPs and gum xanthan based hydrogels nanocomposites for the efficient capture of malachite green from aqueous solution. Chem. Eng. 255: 471-482. https://doi.org/10.1016/j.cej.2014.04.098.

[13] Prajwal K, Vishalakshi B (2020) Efficient removal of dyes and heavy metal ions from waste water using Gum ghatti – *graft* – poly(4-acryloylmorpholine) hydrogel incorporated with magnetite nanoparticles J. Environ. 8: 104207. https://doi.org/10.1016/j.jece.2020.104207.

[14] Preetha BK, Vishalakshi B (2019) Karaya gum-graft-poly(2-(dimethylamino)ethyl methacrylate) gel: an efficient adsorbent for removal of ionic dyes from water. Int. J. Biol. Macromol. 122: 997-1007. https://doi.org/10.1016/j.ijbiomac.2018.09.038.

[15] Mahto A, Mishra S (2021) Guar gum rafted itaconic acid: a solution for different waste water treatment. J. Polym. Environ. https://doi.org/10.1007/s10924-021-02125-2.

[16] Gangadhar B, Vishalakshi B (2019) Silver nanoparticles embedded pectin-based hydrogel: a novel adsorbent material for separation of cationic dyes. Polym. Bull. 76: 4215-4236. https://doi.org/10.1007/s00289-018-2584-7.

[17] Radi S, El Abiad C, Carvalho AP, Santos SM, Faustino MAF, Neves PMS, Moura NMM (2018) An efficient hybrid adsorbent based on silica-supported amino penta-carboxylic acid for water purification. J. Mater. Chem. A 27: 13096–13109. https://doi.org/10.1039/C8TA02560F.

[18] Lazar MM, Dinu IA, Silion M, Dragan ES, Dinu MV (2019) Could the porous chitosan-based composite materials have a chance to a ‘‘NEW LIFE” after Cu(II) ion binding? Int. J. Biol. Macromol. 131: 134–146. https://doi.org/10.1016/j.ijbiomac.2019.03.055.

[19] Anush SM, Vishalakshi B (2019) Modified chitosan gel incorporated with magnetic nanoparticle for removal of Cu(II) and Cr(VI) from aqueous solution. Int. J. Biol. Macromol. 133: 1051-1062. https://doi.org/10.1016/j.ijbiomac.2019.04.179.

[20] Anush SM, Chandan HR, Vishalakshi B (2019) Synthesis and metal ion adsorption characteristics of graphene oxide incorporated chitosan Schiff base. Int. J. Biol. Macromol. 126: 908-916. https://doi.org/10.1016/j.ijbiomac.2018.12.164.

[21] Anush SM, Chandan HR, Gayathri BH, Asma, Manju N, Kalluraya B, Vishalakshi B (2020) Graphene oxide functionalized chitosan-magnetite nanocomposite for removal of cu(II) and Cr(VI) from waste water. Int. J. Biol. Macromol. 164: 4391-4402. https://doi.org/10.1016/j.ijbiomac.2020.09.059.

[22] Ahmad S, Ahmad M, Manzoor K, Purwar R, Ikram S (2019) A review on latest innovations in natural gums based hydrogels: preparations & applications. Int. J. Biol. Macromol. 136: 870-890. https://doi.org/10.1016/j.ijbiomac.2019.06.113.

[23] Singh B, Abhishek D (2017) Evaluation of gentamicin and lidocaine release profile from gum acacia-crosslinked-poly(2-hydroxyethylmethacrylate)-carbopol based hydrogels. Curr. Drug. Deliv. 14: 981-991. https://doi.org/10.2174/1567201814666170127163715.

[24] Sharma G, Kumar A, Naushad M, Garcia-Penas A, Al-Muhtaseb AH, Ghfar AA, Sharma V, Ahamad T, Stadler FJ (2018) Fabrication and characterization of gum arabic-cl-poly(acrylamide) nanohydrogel for effective adsorption of crystal violet dye. Carbohydr. Polym. 202: 444-453. https://doi.org/10.1016/j.carbpol.2018.09.004.

[25] Abdel-Bary EM, Elbedwehy AM (2018) Graft copolymerization of polyacrylic acid onto acacia gum using erythrosine–thiourea as a visible light photoinitiator: application for dye removal. Polym. Bull. 75: 3325–3340. https://doi.org/10.1007/s00289-017-2205-x.

[26] Elbedwehy AM, Abou-Elanwar AM, Ezzat AO, Atta AM (2019) Super effective removal of toxic metals water pollutants using multi functionalized polyacrylonitrile and arabic gum grafts. Polymers 11: 1938. https://doi.org/10.3390/polym11121938.

[27] Sun P, Hui C, Khan AR, Du J, Zhang Q, Zhaoa YH (2015) Efficient removal of crystal violet using Fe_3O_4-coated biochar: the role of the Fe_3O_4 nanoparticles and modeling study their adsorption behavior. Sci. Rep. 5: 12638–12649. https://doi.org/10.1038/srep12638.

[28] Pourjavadi A, Hosseini SH, Seidi F, Soleyman R (2013) Magnetic removal of crystal violet from aqueous solutions using polysaccharide-based magnetic nanocomposite hydrogels. Polym. Int. 62: 1038–1044. https://doi.org/10.1002/pi.4389.

[29] Hossan MS, Ochiai B (2018) Preparation of TiO_2-poly(3-chloro-2-hydroxypropylmethacrylate) nanocomposite for selective adsorption and degradation of dyes. Technologies 6: 92. https://doi.org/10.3390/technologies6040092.

[30] Reddy NN, Mohan YM, Varaprasad K, Ravindra S, Joy PA, Raju KM (2011) Magnetic and electric responsive hydrogel–magnetic nanocomposites for drug-delivery application. J. Appl. Polym. Sci. 122: 1364–1375. https://doi.org/10.1002/app.34016.

[31] Mahdavi M, Ahmad MB, Haron MJ, Namvar F, Nadi B, Rahman MZA, Amin J (2013) Synthesis, surface modification and characterization of biocompatible magnetic iron oxide nanoparticles for biomedical applications. Molecules 18: 7533-7548. https://doi.org/10.3390/molecules18077533.

[32] Sing KSW, Everett DH, Haul RAW, Moscou L, Pierotti RA, Rouquerol J, Siemieniewska T (2008) Reporting physisorption data for gas/solid systems. Pure Appl. Chem. 57: 603–661. https://doi.org/10.1002/9783527610044.hetcat0065.

[33] Prajwal K, Vishalakshi B (2020) Hybrid nanocomposite of kappa-carrageenan and magnetite as adsorbent material for water purification. Int. J. Biol. Macromol. 165: 542-553. https://doi.org/10.1016/j.ijbiomac.2020.09.202.

[34] Mittal H, Kumar V, Ray SS, Saruchi (2016) Adsorption of methyl violet from aqueous solution using gum xanthan/Fe_3O_4 based nanocomposite hydrogel. Int. J. Biol. Macromol. 89: 1–11. https://doi.org/10.1016/j.ijbiomac.2016.04.050.

[35] Akbarzadeh A, Samiei M, Davaran S (2012) Magnetic nanoparticles: preparation, physical properties, and applications in biomedicine. Nanoscale Res. Lett. 7: 144. https://doi.org/10.1186/1556-276X-7-144.

[36] Prajwal K, Vishalakshi B (2020) Magnetite nanoparticle embedded pectin-graft-poly(N-hydroxyethylacrylamide) hydrogel: evaluation as adsorbent for dyes and heavy metal ions from waste water. Int. J. Biol. Macromol. 156: 1408–1417. https://doi.org/10.1016/j.ijbiomac.2019.11.181.

[37] Zeng Q , Qi X, Zang M, Tong X, Jiang N, Pan W, Xiong W, Li Y, Xu J, Shen J, Xu L (2020) Efficient decontamination of heavy metals from aqueous solution using pullulan/polydopamine hydrogels. Int. J. Biol. Macromol. 145: 1049–1058. https://doi.org/10.1016/j.ijbiomac.2019.09.197.

[38] Ayawei N, Ebelegi AN, Wankasi D (2017) Modelling and interpretation of adsorption isotherms. J. Chem. 2017: 1-11. https://doi.org/10.1155/2017/303981.

[39] Freundlich H (1926) Colloid and capillary chemistry. J. Soc. Chem. Ind. 45: 797–798. https:// doi.org/10.1002/jctb.5000454407.

[40] Lagergren S (1898) About the theory of so called adsorption of soluble substances. Handlingar 24: 1–39. https://doi.org/10.12691/ijebb-4-2-4.

[41] Ho YS, McKay G (1999) Pseudo-second order model for sorption processes. Process Biochem. 34: 451–465. https://doi.org/10.1016/S0032-9592(98)00112-5.

[42] Ilgin P, Ozay H, Ozay O (2019) Selective adsorption of cationic dyes from colored noxious effluent using a novel N-tert-butylmaleamic acid based hydrogels. React. Funct. Polym. 142: 189–198. https://doi.org/10.1016/J.REACTFUNCTPOLYM.2019. 06.018.

[43] Pour ZS, Ghaemy M (2015) Removal of dyes and heavy metal ions from water by magnetic hydrogel beads based on poly(vinyl alcohol)/carboxymethyl starch-g-poly (vinyl imidazole). RSC Adv. 5: 64106–64118. https://doi.org/10.1039/ C5RA08025H.

[44] Mittal H, Morajkar PP, Alhassan SM (2020) In-situ synthesis of ZnO nanoparticles using gum arabic baesd hydrogels as a self-template for effective malachite green dye adsorption. J. Polym. Environ. 28: 1637-1653. https://doi.org/10.1007/s10924-020-01713-y.

[45] Banerjee SS, Chen DH (2007) Fast removal of copper ions by gum arabic modified magnetic nano-adsorbent. J. Hazard. Mater. 147: 792-799. https://doi.org/10.1016/j.jhazmat.2007.01.079.

[46] Iftekhar S, Srivastava V, Casas A, Sillanpa M (2018) Synthesis of novel GA-g-PAM/SiO_2 nanocomposite for the recovery of rare earth elements (REE) ions from aqueous solution. J. Clean. Prod. 170: 251-259. https://doi.org/10.1016/j.jclepro.2017.09.166.

Declaration of interest

None

Figures

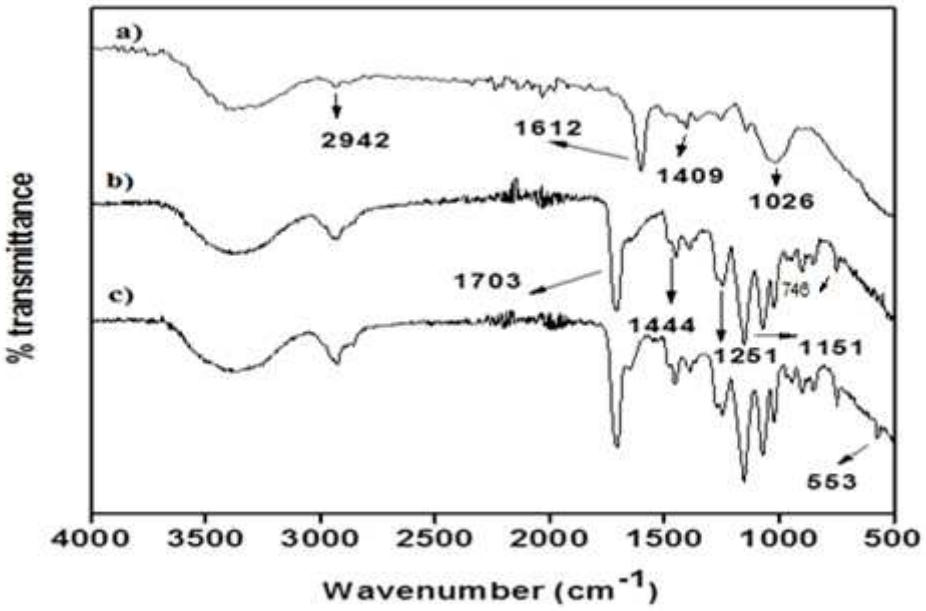

Figure 1

FTIR spectra of a) GA b) GA-g-PCHPMA c) GA-g-PCHPMA/Fe3O4

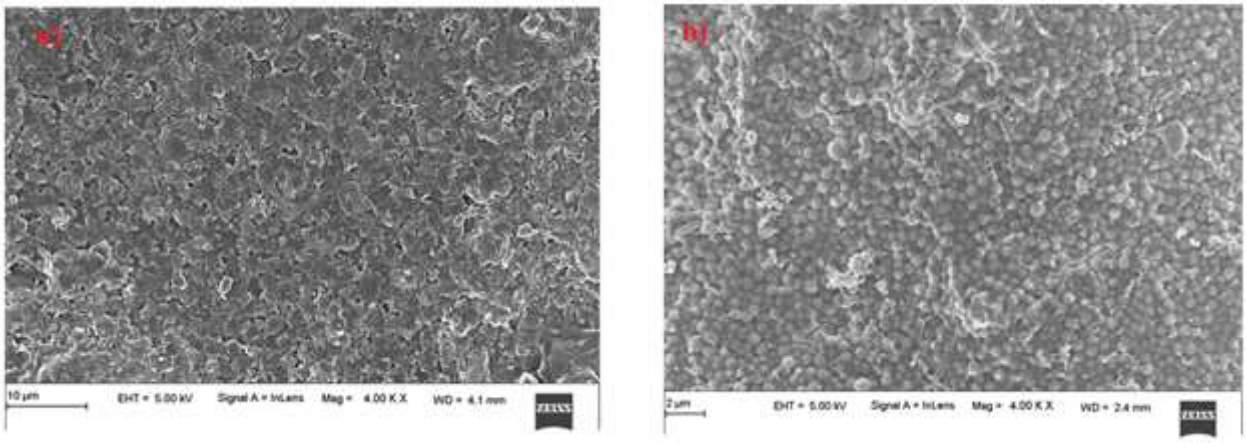

Figure 2

SEM images of a) GA-g-PCHPMA b) GA-g-PCHPMA/Fe3O4

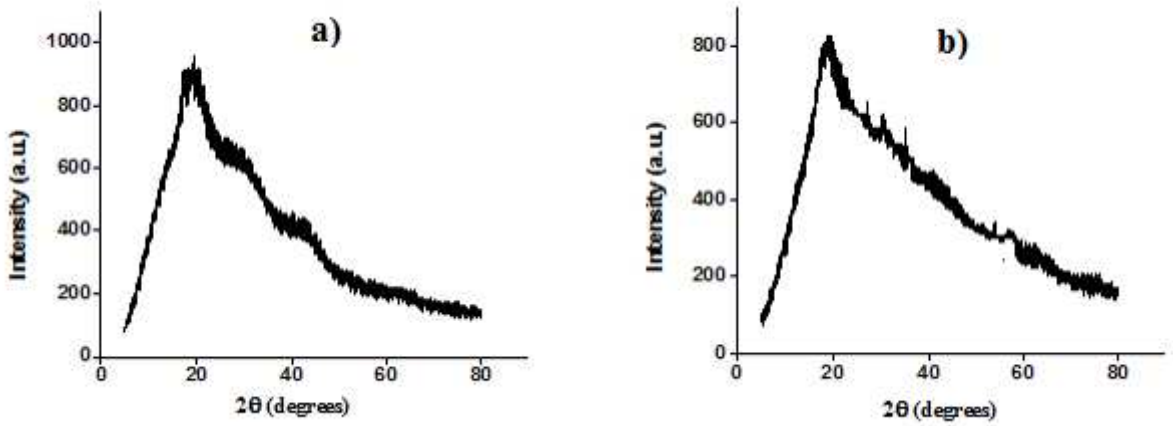

Figure 3

XRD patterns of a) GA-g-PCHPMA b) GA-g-PCHPMA/Fe3O4

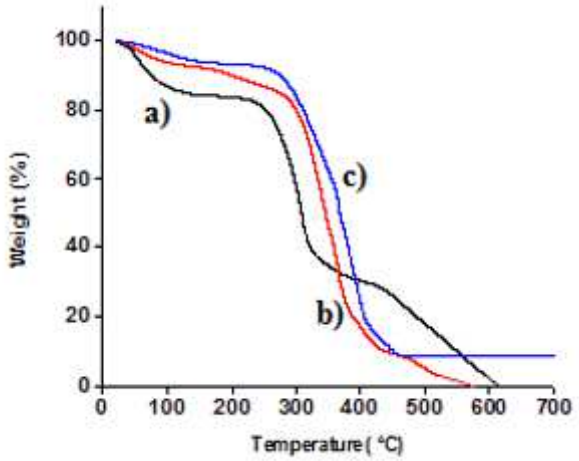

Figure 4

TGA curves of a) GA b) GA-g-PCHPMA c) GA-g-PCHPMA/Fe3O4

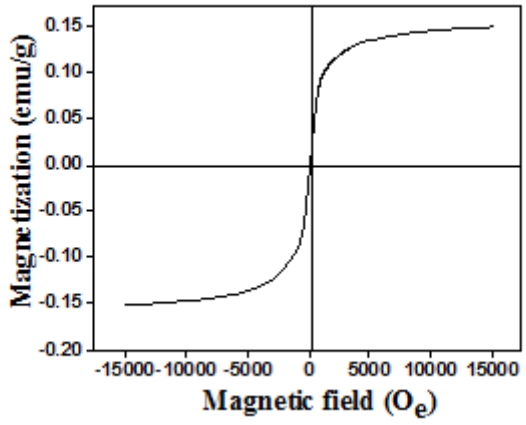

Figure 5

Magnetization curve of GA-g-PCHPMA/Fe3O4 at room temperature

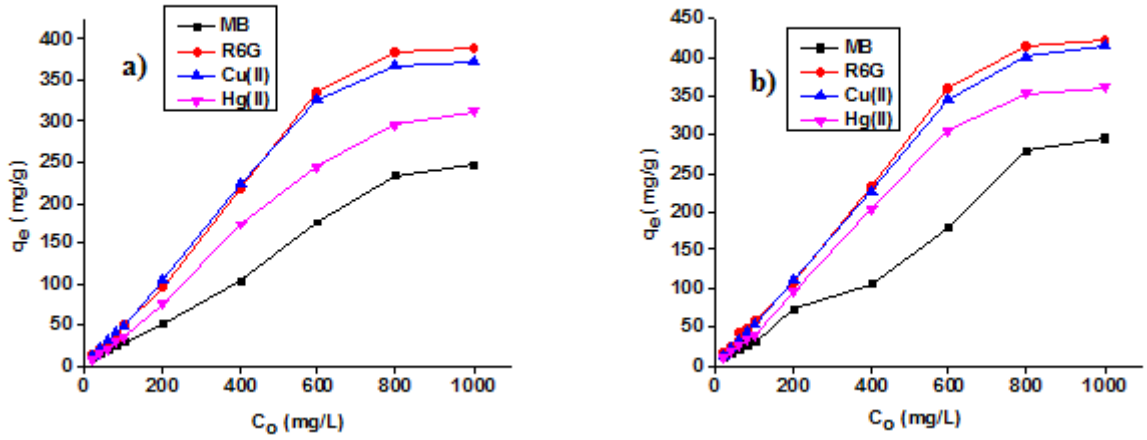

Figure 6

The effect of initial concentration of dyes and metal ions on adsorption for a) GA-g-PCHPMA b) GA-g-PCHPMA/Fe3O4 (t = 4 hrs, T =30oC)

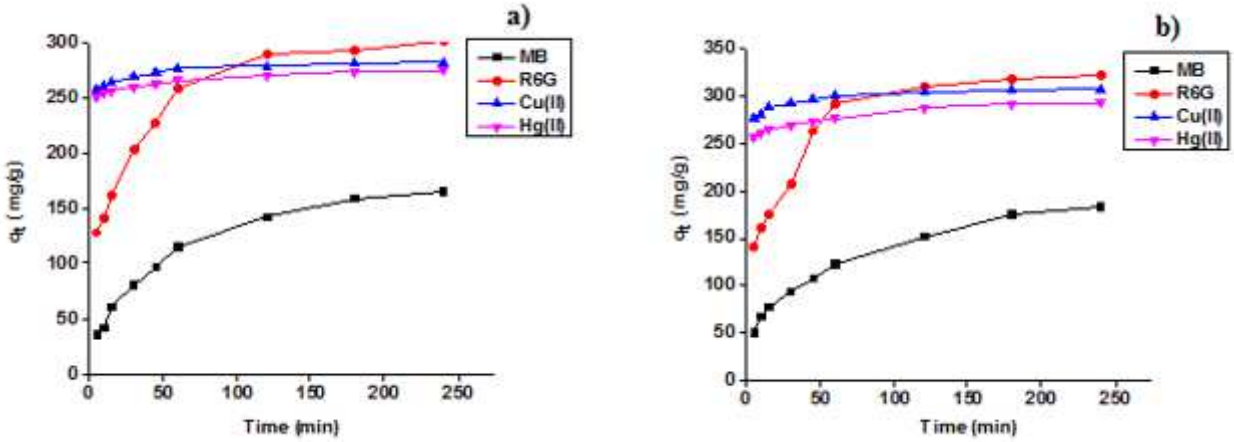

Figure 7

The effect of contact time on the adsorption of dyes and metal ions on a) GA-g-PCHPMA b) GA-g-PCHPMA/Fe3O4 (Co = 500 mg/L, T =30oC)

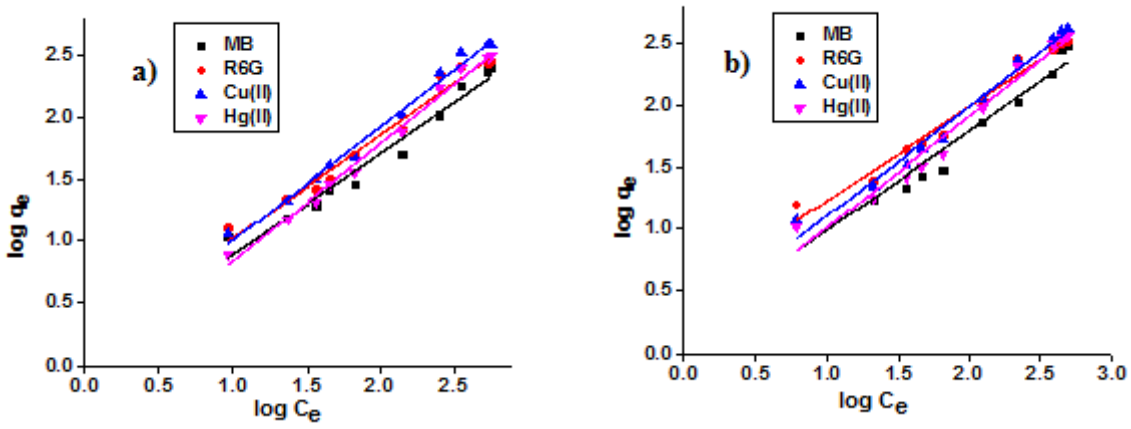

Figure 8

Freundlich isotherm model fit for the adsorption of dyes and metal ions on a) GA–g–PCHPMA and b) GA–g–PCHPMA/Fe3O4

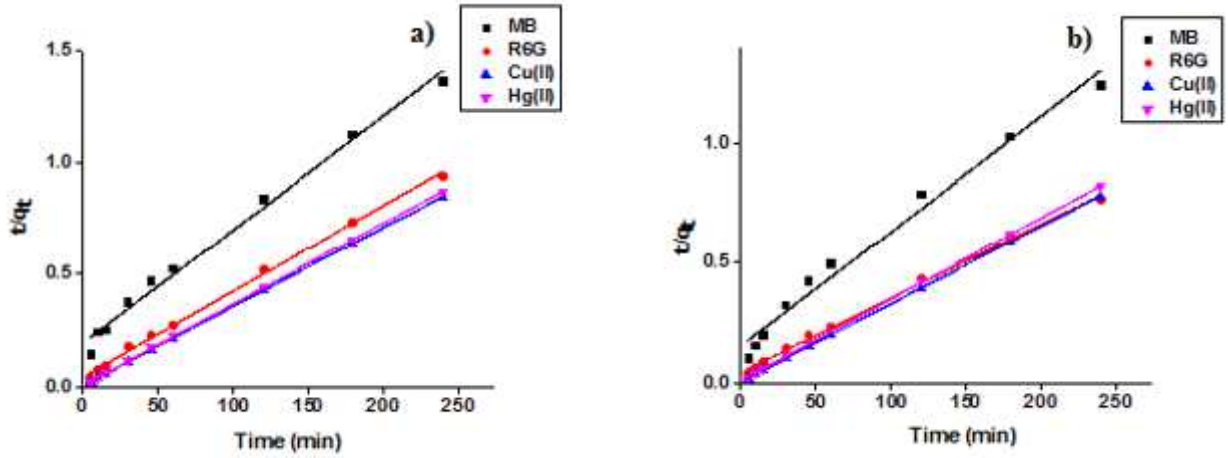

Figure 9

Pseudo second order kinetic plot for adsorption of dyes and metal ions on a) GA–g–PCHPMA b) GA–g–PCHPMA/Fe3O4

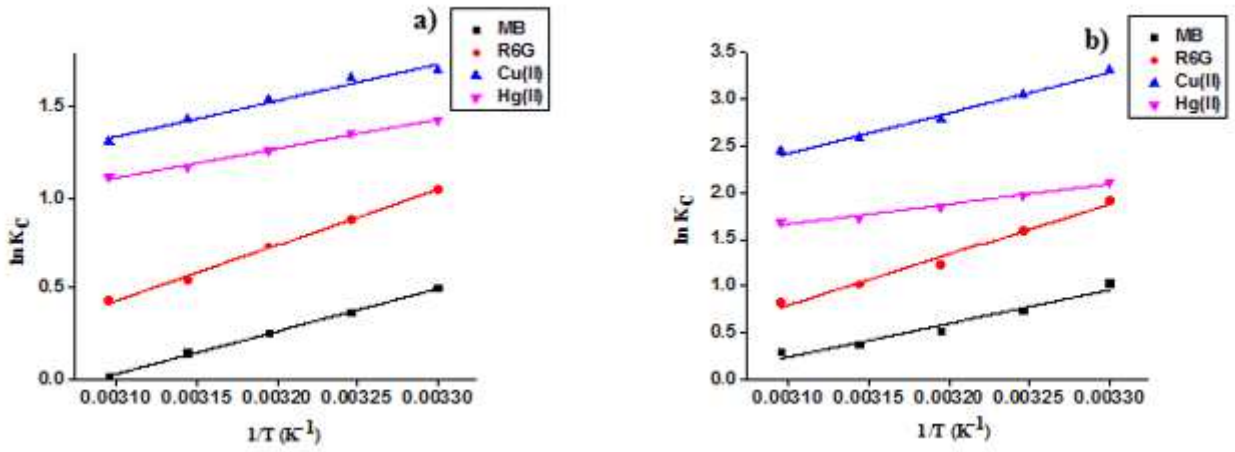

Figure 10

Plot of ln KC vs 1/T for the uptake of dyes and metal ions on a) GA–g–PCHPMA and b) GA–g–PCHPMA/Fe3O4

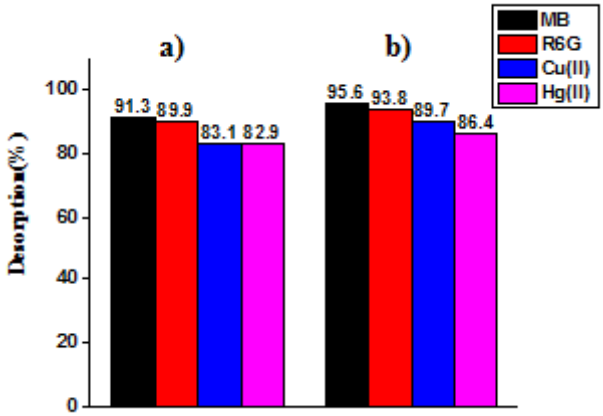

Figure 11

Desorption (%) of dyes and metal ions from a) GA–g–PCHPMA and b) GA–g–PCHPMA/Fe3O4

Supplementary Files

This is a list of supplementary files associated with this preprint. Click to download.

- SupportingInformation.docx
- Figures.docx
- Tables.docx